Discrete & Continuous Models
& Applied Computational Science
ISSN 2658-7149 (Online), 2658-4670 (Print)

2024, 32 (2) 181–201
http://journals.rudn.ru/miph

Review

UDC 004.2, 004.7
PACS 07.05.Tp
DOI: 10.22363/2658-4670-2024-32-2-181–201 EDN: CFLJNF

The recent progress in terahertz channel characterization and system design

Alexander S. Shurakov[1,2], Evgeny V. Mokrov[3], Anatoliy N. Prikhodko[1,2,4], Margarita I. Ershova[1], Vyacheslav O. Begishev[3], Abdukodir A. Khakimov[3], Yevgeny A. Koucheryavy[3], Gregory N. Gol'tsman[1,2,4]

[1] *Moscow Pedagogical State University, 1 M. Pirogovskaya St, bldg. 1, Moscow, 119991, Russian Federation*
[2] *HSE University, 20 Myasnitskaya St, Moscow, 101000, Russian Federation*
[3] *RUDN University, 6 Miklukho-Maklaya St, Moscow, 117198, Russian Federation*
[4] *Russian Quantum Center, Skolkovo, 143025, Russian Federation*

(received: March 25, 2024; revised: April 10, 2024; accepted: April 15, 2024)

Abstract. As the standardization of 5G New Radio (NR) systems operating in micro- and millimeter-wave frequency bands is over, scientific and industrial communities have begun to address the question of what 6G communications systems might or should be. While technological specifics are still in their early development phase, there is a common agreement that these systems will utilize the lower part of the terahertz band, namely, 100–300 GHz. This band poses a number of specific challenges for system designers, including the effects related to channel characteristics and the conceptually new requirements for electronics. This paper aims to report the current state-of-the-art channel characterization and communications system design. With respect to the former, we consider dynamic human body blockages and micromobility impairments. For the latter, we mainly concentrate on the physical layer devices for direct conversion schemes and the design of the so-called reconfigurable intelligent surfaces that will potentially serve as a cost-efficient blockage mitigation technique.

Key words and phrases: terahertz band, 6G, dynamic blockage, micromobility, experiment, coherent communication, direct conversion, reconfigurable intelligent surface

Citation: Shurakov A. S., Mokrov E. V., Prikhodko A. N., Ershova M. I., Begishev V. O., Khakimov A. A., Koucheryavy Y. A., Gol'tsman G. N., The recent progress in terahertz channel characterization and system design. *Discrete and Continuous Models and Applied Computational Science* **32** (2), 181–201. doi: 10.22363/2658-4670-2024-32-2-181–201. edn: CFLJNF (2024).

1. Introduction

Expanding the available bandwidth is the main tool for increasing rates at the access interface in cellular systems. This trend has been in place since 3G systems with 3G UMTS, 4G LTE, and 5G NR utilizing 2 MHz, 20 MHz, and 50 MHz wide basic channels, respectively, thus offering higher bandwidth. With 5G New Radio systems operating in the millimeter wave (mmWave, 24–100 GHz) band, the next logical step is the sub-terahertz/terahertz (sub-THz/THz, 100–300 GHz) band and even higher, where enormous yet unregulated bandwidth is available. Such bandwidth may result in data rates potentially supporting a plethora of upcoming applications, including virtual/augmented reality (VR/AR), holographic communications, etc.

The use of the THz band poses several challenges to systems designers. The first set is related to still unsolved propagation effects that were already evident in the mmWave band, including dynamic blockage by human bodies and the micromobility phenomenon. The former makes mmWave/THz systems unusable under the conditions they were invented for large dense crowds generating enormous traffic demands. The solution to this problem requires fast and accurate blockage detection mechanisms and methods to decrease the frequency of blockage events. Micromobility is closely related to the utilization of directional antennas and is expected to become more relevant at THz frequencies, where the directivity of antenna radiation patterns will further increase.

The development of large-scale antenna devices for the front ends of ultra-directional THz transmitters and receivers, as well as the smart 6G antenna environment, must comply with the criteria of cost and power efficiency. Moreover, supporting extremely large bandwidths is another challenge. This solution requires the use of advanced circuits for THz signal generation and processing that are naturally compatible with ultrafast and spectrally effective communication schemes. This, in turn, can be accomplished via partial replacement of intrinsically limited Si-based electronics with more capable A3B5 electronic and radiophotonic devices.

This paper aims to report the recent progress in THz channel characterization and system design. In the former topic, we concentrate on two effects currently affecting the public deployment of mmWave/THz communication systems: dynamic human body blockage and micromobility. In the context of system design, we consider state-of-the-art coherent communications with direct conversion and reconfigurable intelligent surfaces (RISs) for reflection-aided channels. The latter can be utilized as a simple and efficient block avoidance technique.

The remainder of this paper is organized as follows. We begin with the effect of dynamic human body blockage in Section 2. In Section 3, we discuss recent progress in micromobility characterization. Section 4 describes the design of state-of-the-art THz communication systems. Finally, in Section 4.2 we consider a potential blockage avoidance solution for 5G and 6G systems – RISs. Finally, the conclusions are presented in the last section.

2. Dynamic blockage

2.1. Motivation and impact

Dynamic blockage of the propagation path by human bodies is one of the critical factors affecting the performance of THz communications systems. This property was first observed in the mmWave domain, where it was demonstrated to result in 15–25 dB attenuation [1] depending on the propagation conditions and environmental characteristics. The eventual impact of this phenomenon is a drastic drop in the received signal strength resulting in either the downgrading of the utilized modulation and coding scheme (MCS) or outage conditions. Due to an even Shorter wavelength attenuation in the THz band is expected to be even more drastic.

Several methods have been proposed for human body blockage avoidance. First, because of the inherent multi-path propagation at mmWave/THz frequencies, a non-line-of-sight (nLoS) path can be utilized for continuing service in the case of blockage. When no outage is experienced bandwidth reservation techniques may still support the active session as proposed in [2, 3]. However, as indicated in the 3GPP TR 38.901 standard, even at mmWave frequencies these paths generally generate less than 10% of the LoS path power. When blockage leads to an outage, multi-connectivity functionality standardized by 3GPP can be utilized [4, 5]. However, this approach requires dense deployment of mmWave/THz base stations (BS), which may not be available during the first deployment phases. In

addition, even when both approaches are utilized together including the implementation of multi-connectivity between mmWave and THz radio access technologies (RAT), there is still a non-negligible probability that a session initially accepted for service will eventually be lost as a result of blockage. Finally, an alternative method is to embed blockage avoidance techniques in the physical layer by utilizing beam focusing [6] and/or non-diffractive beams [7]. However, these studies are still in their infancy.

Blockage detection techniques are required to enforce blockage avoidance. These techniques can be classified as proactive and reactive techniques [8]. However, for both one needs to understand not only the duration of the blockage periods but also the duration of the signal fall and rise times. The signal fall time is of critical importance as it is not allowed to benchmark the development test but can serve as an indicator of the type of impairment allowing to distinguish blockage from other events including fast fading and/or micromobility discussed in Section 3.

2.2. Related work

In this section, we outline related studies that characterize the impact of dynamic human body blockages in the THz band. We start by briefly reviewing the results of the LoS path propagation and blockage.

First, we highlight a notable deficiency in the current body of research on propagation phenomena beyond the 100 GHz. Studies on the attenuation and time dynamics of the blockage process remain scarce. For instance, [9] provides an overview of propagation loss measurements at 140 GHz for various building materials: however, the characteristics of the blockage process have not been reported. The authors of [10, 11] reported attenuation values for 300 GHz for vehicular blockage in different configurations, but these results cannot be extrapolated to human body blockage owing to the different materials and geometries.

Numerous authors have investigated the transparency characteristics of materials, as evidenced in [9, 12, 13]. For example, [14] explored the attenuation induced by various materials in the sub-THz range, whereas [12] reported measurements at four different frequencies, with two considered to belong to the sub-THz range. The study in [15] presented an analytical model based on the average blockage probability estimated empirically as follows a function of the relative positions of the receiver (Rx) and transmitter (Tx), average Tx/Rx heights, antenna parameters, and room size.

In general, despite the existing body of data regarding the penetration of sub-THz signals through diverse materials and measurement campaigns related to vehicular communications, a comprehensive characterization of the human body attenuation process within the sub-THz frequency spectrum is lacking. This is especially concerning for the signal fall and rise times.

2.3. Recent results

The first step towards this direction was taken in [8], where the authors investigated the signal blockage by the human body at a frequency of 156 GHz in the indoor environment, as shown in Fig. 2a. An example of the signal behavior under blockage is shown in Fig. 1, where it is marked by a ”direct trace”. The authors focused on blockage characteristics, including average signal attenuation and timing metrics such as signal fall and rise times, and blockage duration. For transmission over a distance of 3–7 m, the average attenuation was found to range from 8 to 15 dB depending on the LoS height and the distance between the Tx and Rx. The blockage duration varied from 5 to 10% for different Tx-Rx distances (with corresponding nominal values of 360–390 ms), while the rise and fall times of the signal gradually increased from 60 to 100 ms as the Tx-Rx distance increased and remained unchanged for different LoS altitudes.

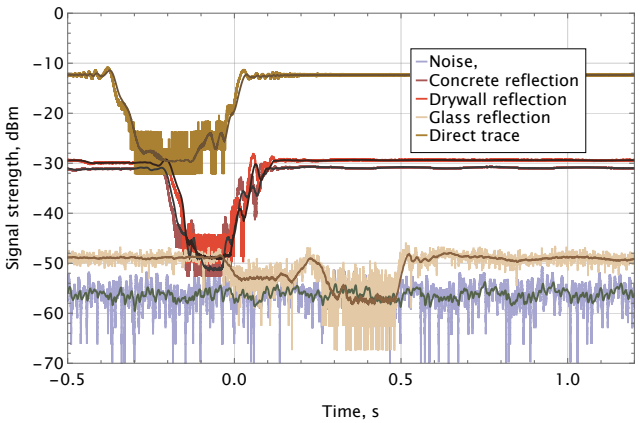

Figure 1. Signal behavior under blockage for straight and reflected propagation

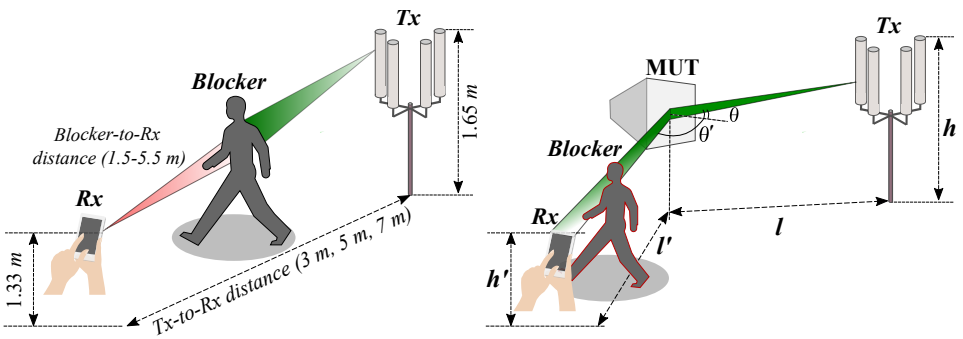

(a) LoS propagation

(b) Reflected propagation

Figure 2. Illustrating considerations in LoS and reflective propagation

In [16], the authors investigated the effect of dynamic blockage by the human body on the signal strength in a highly directive channel in the sub-THz frequency range under typical indoor conditions with reflection from different materials, as shown in Fig. 2b. An illustration of the blocked signal under the reflected propagation of different materials is shown in Fig. 1. Through an extensive measurement campaign at the 156 GHz carrier frequency, reflection and blocking losses along various nLoS paths were reported, as well as the corresponding blockage duration, fall, and rise times. Empirical studies were validated using material-dependent 156 GHz radio propagation models for 24 different measurement configurations.

Upon visual examination of Fig. 1, it is clear that signal levels received from paths involving reflection in unobstructed conditions are notably lower than those of direct line-of-sight paths. This discrepancy is primarily attributed to the losses incurred during reflection. Additionally, distinct variations were observed in both obstruction patterns and signal strengths both preceding and following the occurrence of an obstruction event. It is also visible that the plots representing the incidence of radio signals are closely clustered together, almost overlapping, particularly in the case of concrete and drywall. Any slight disparities observed, especially in the case of glass, can likely be

Table 1

Mean signal attenuation, fall, and rise times

LoS propagation			
Tx-RX distance, *m*	Attenuation, dB	Rise time, ms	Fall time, ms
3 m	13.87	59.26	62.39
5 m	12.16	85.73	79.17
7 m	7.29	102.51	95.57
Reflected propagation, 3 m Tx-Rx distance			
Type of material	Attenuation, dB	Rise time, ms	Fall time, ms
Concrete	11.59	51.615	67.475
Drywall	11.15	46.231	53.186
Glass	9.76	44.081	39.338

ascribed to external variables such as the dynamic range of the Rx and the consistency of the motion trajectories of the obstructions.

Table 1 summarizes the results in [8, 16] for signal attenuation, fall, and rise times. The presented results show notice that the presence of reflection does not quantitatively change the mean signal attenuation as it remains in the range of 10–13 dB. For LoS propagation conditions the mean signal fall time varied between 60–90 ms depending on the propagation distance. The type of reflecting material affects these values. Specifically, for glass, it becomes as small as 39 ms. Even for 5G mmWave NR technology, the time gap is at least a few frames making it possible to utilize reactive blockage detection tests for multiconnectivity operations.

3. Micromobility

3.1. Motivation and impact

Modern 5G NR and future 6G cellular systems operate using antenna arrays. The use of directional antenna radiation patterns requires a beam-tracking procedure. For example, in 5G NR systems, beam tracking is performed regularly every 10–320 ms, where the actual interval is chosen by the network operator. Because of the much smaller wavelength in the 100–3000 GHz band, the half-power beamwidth (HPBW) of antenna arrays in 6G systems is substantially higher than that of 5G NR systems. This increase leads to extreme overhead in terms of (i) the time needed to perform beam tracking, (ii) frequency resources, and (iii) energy.

In terms of power, it has been shown that although the power consumption induced by beam tracking is smaller than that caused by the actual data transmission, it still adds significant overheads, especially for low data rate applications having intermittent connectivity such as web browsing [17]. The time required to find the best antenna configuration is directly proportional to the number of antenna array elements on the BS and UE sides. That is when hierarchical beam searching is utilized, as $(N_B + N_U)\delta$, where δ is the array switching time ($2 - 10\mu$s for modern arrays), N_B and N_U are the numbers of antenna configurations at the BS and UE sides, respectively. In terms of frequency resources, the overhead also scales proportionally with the number of Synchronization Signal Blocks

(SSB) per frame

$$R_O = \frac{N_{pss} + N_{sss} + N_{pbch} + N_{ssb}}{N_{rb} + N_{sc} + N_{sl} + N_{sym}},$$

where N_{sym} is the number of symbols in a slot, N_{sl} is the number of slots per frame, N_{sc} is the number of sub-carriers, N_{rb} is the total number of resource blocks (RB), N_{ssb} is the number of SSB per frame, N_{pbch} is the number of primary broadcast channel resource elements (RE), N_{sss} is the number of secondary synchronization signal REs, N_{pss} is the number of primary synchronization signal REs. Since the HPBW of the antenna array can be approximated by $102°/N$ [18] and assuming sectoral coverage of a single BS antenna, N_{ssb} can be approximated as $N_{ssb} = 120°(N_B + N_U)^2/102° = 1.18(N_B + N_U)^2$ implying quadratic dependence.

These overheads imply that the interval between the beam-tracking time instants must be minimized. In current 5G NR systems regular beam tracking is utilized with the interval between synchronization time instants set at the BS and UE and between 10 ms and 320 ms. Moving forward towards 6G systems such timings may become infeasible owing to the considered overheads, and thus, there is a need to optimize the time interval between beam tracking time instants.

3.2. Related work

The effect of micromobility is inherent to systems with directional antennas. Although 5G NR systems already utilize directional antenna radiation patterns the HPBW of the antenna arrays is rather large for micromobility to produce a noticeable impact. Nevertheless, it has already been experimentally characterized for 5G NR systems in [19], where the authors demonstrated that it may lead to degradation of the received signal strength.

As we move towards the THz band, the dimensions of the antenna arrays grow, leading to a higher HPBW directivity. The seminal work on, where the impact of user micromobility on link performance was characterized in [20]. The authors utilized inertial sensors embedded in a smartphone including a gyroscope and accelerometer to characterize the stochastic trajectories of the imaginary boresight of the beam. Shows the basic trade-off between outage time and spectral efficiency for different HPBW sizes. Furthermore in [21], the same authors utilized simple micromobility models based on diffusion processes to assess the performance of on-demand and regular beam-tracking procedures in the THz band. Their results illustrate that the latter, which is currently utilized for 5G NR systems, may not be the best option when the number of antenna elements reaches a level that is typical for 6G THz systems.

The authors in [22] carried out a micromobility emulation, where the boresight of the beam was represented by a laser pointer firmly connected to the smartphone. They considered four types of applications including video watching, VR watching, racing games, and phone calling, and demonstrated that the different types of applications are characterized by different micromobility properties. They also showed that some applications such as video watching and phone calling may allow for large times between beam tracking time instants. In [22], based on the statistical data obtained in [23], three models were formulated and parameterized: (i) two-dimensional Markov model, (ii) decomposed over Oy and Ox axes one-dimensional Markov model, and (iii) decomposed over Oy and Ox axis Brownian motion model. The models were compared using the time to outage after the beam-tracking time instant. The results demonstrated that the two-dimensional Markov model produced the best approximation of the considered metric but was characterized by the highest complexity as the number of states reached thousands. On the other hand, decomposed models are suitable as first-order approximations for those applications, where the user actions are not explicitly controlled by the application, for example, all applications excluding racing games.

Once the effect of micromobility has been characterized, studies assessing its impact on user- and system-level performance, as well as proposing solutions for remote application detection, have started to appear. First, in [24], the authors characterized the impact of micromobility on the outage performance of 6G THz systems with micromobility functionality. They demonstrated to achieve a meaningful compromise between outage and spectral efficiency the beam searching time must be decreased by at least ten times. This can be achieved by utilizing a faster switching time of the antenna configuration. Furthermore, in [5], a joint deployment of mmWave and THz 6G communication systems was considered. By accounting for both channel- and resource-dependent factors, the authors demonstrated that a system with intermittent connectivity induced by micromobility must rely on fully reliable backup options such as 4G LTE.

With respect to the applications classification for maximizing the time between beam-tracking time instants, the authors in [25] advocated the use of inertial sensors including gyroscopes and accelerometers to decrease the search space for antenna configurations on both the BS and UE sides. However, as shown by the authors, the inaccuracy of modern embedded sensors is insufficient for achieving sufficient gains in terms of the time spent searching for beams. An alternative approach based on the boresight of the antenna main lobe detection was proposed in [26]. Although nearly perfect application detection can be achieved which may result in optimal beam tracking intervals, the considered metric (boresight location) is not immediately available at the BS and UE sides.

Despite significant efforts to date, there are neither measurements nor methodologies that characterize the impact of micromobility on the received signal strength immediately after the beam tracking time instant.

3.3. Measurements methodology

Owing to the lack of miniaturized equipment operating in the sub-THz frequency band, to carry out the micromobility measurement campaign we applied the following multi-stage methodology: (i) beam center mobility emulation for different applications, (ii) Markov modeling of the time-series, (iii) generation of control traces for real measurements, and (iv) actual micromobility measurements in the sub-THz band.

Beam center micromobility emulation. In the first stage, we emulated the micromobility of the beam center using a laser pointer firmly fixed to the UE. A user utilizes UE to run applications including (i) racing games, (ii) phone calls, (iii) VR watching, and (iv) video watching. A large white screen is used to track the moving spot produced by the laser. A high-resolution camera operating at 120 fps was used to capture the time-dependent position of the laser spot. Standard signal processing techniques were utilized to convert the stop location to grid coordinates. Overall, we performed 10 independent measurements for four considered applications. The duration of each measurement was set to 120 seconds. Additional details of the experimental setup are provided in [23].

Markov modeling of time-series. Once the traces were collected, we developed models for the time series. To explicitly capture both distributional and correlational properties, we utilized a two-dimensional Markov chain framework. Accordingly, the entire range of the x and y coordinates was divided into $N \times N$ cells. The transition probabilities were then calculated to produce the Markov model. The value of N can be tuned based on the required model accuracy. Based on the analysis conducted in [23], the value of $N = 100$ was chosen. The accuracy of the model was assessed in [22], where the reported results demonstrated that it performs better than simplified models including decomposed Markov and Brownian motion models.

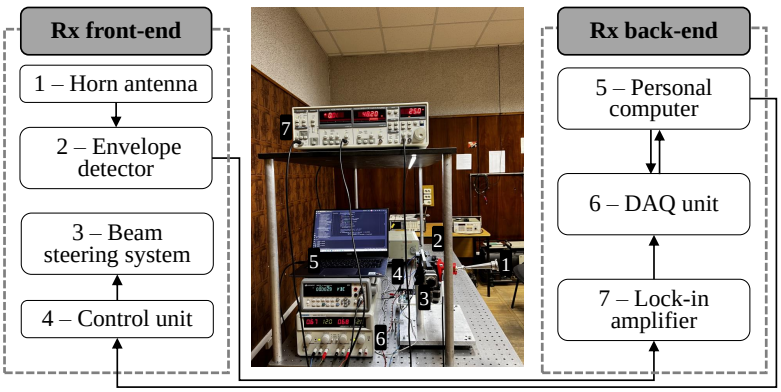

Figure 3. Schematic diagram and photograph of a steerable Rx

Control traces generation. In real measurements of the received signal strength affected by the micromobility patterns we utilized high-precision goniometers to control the direction of the antenna. We utilized the specified models to generate control traces consisting of 0s and 1s indicating positive and negative, respectively, steps for the vertical and horizontal planes. Note that the maximum time resolution of the goniometers was 150 ms/° which was slower than the micromobility speed of the racing game and VR-watching applications. To this end, we utilized the time expansion technique to align the maximum speed of the applications with that of the goniometers. The reverse procedure was implemented to restore the actual time after the measurements were performed.

Micromobility measurement campaign. The experimental setup consisted of two key components: a static transmitting module (Tx) and a mobile receiving module (Rx). The first is based on a solid-state source comprising a microwave synthesizer, followed by a sub-THz frequency multiplication chain (FMC). The Tx provides 44 mW of output power in the form of a modulated constant waveform with a modulation frequency of 25 kHz at a carrier frequency of 156 GHz. The voltage-controllable attenuator terminating the FMC provides strict amplitude control of the Tx-generated signal and performs the function of a modulator. It was also synchronized with a lock-in amplifier used at the back end of the Rx (Fig. 3). The Rx front end included a waveguide envelope detector based on a Schottky diode with 100 V/W of responsivity. The detector is equipped with a high-directivity horn antenna identical to that of Tx and is integrated with a beam steering system consisting of two motorized single-axis goniometers. The control traces used to drive the goniometers along the predefined angular trajectories have the form of matrices containing four columns with 0s and 1s (the generation procedures are provided earlier in the text). The values from the first and third columns are responsible for changing the direction of the instantaneous angular step of each goniometer (1—positive, 0—negative), the second and fourth, in turn, – for the corresponding magnitudes of the angular steps (1—24.8 arc seconds, 0—0 arc seconds). From a personal computer, the traces are submitted to control and data acquisition (DAQ) units synchronizing the transmission and directive reception of the sub-THz signal. Rx was placed 400 cm away from Tx such that their optical axes were co-aligned at the beginning of each measurement. The recorded time series of the received signal strength is statistically processed.

Time-series. The selected time-series of signal strength impaired by the micromobility of applications is shown in Fig. 4. The visual analysis of the observed data shows that one application stands out from the rest – video watching is characterized by extremely steady behavior with signal strength remaining close to the maximum even after significant time after beam alignment. On some

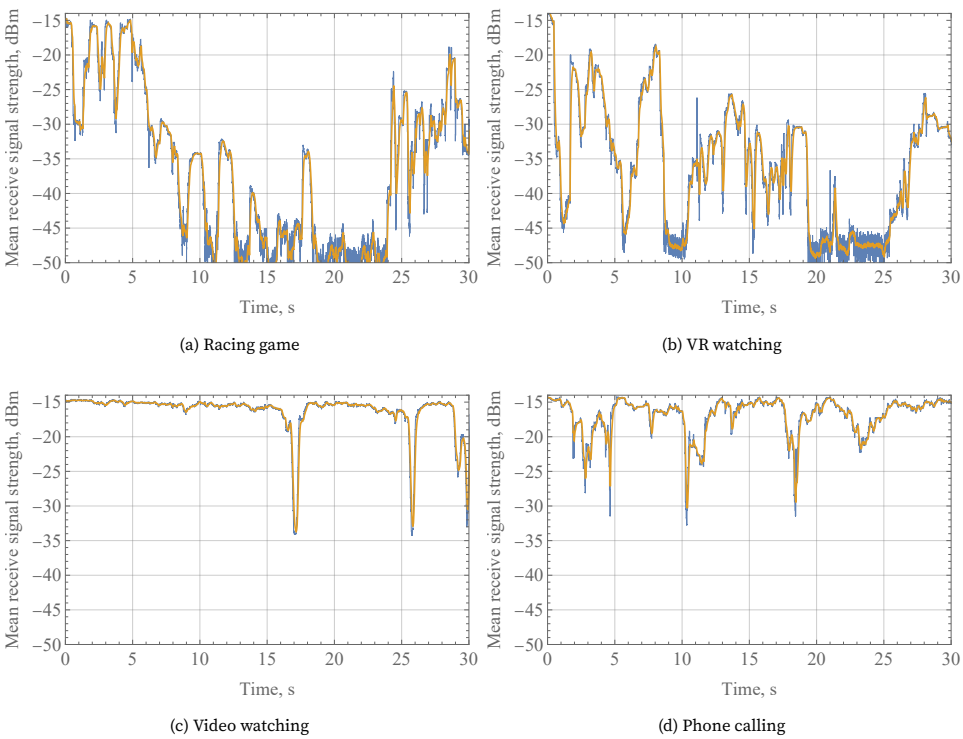

(a) Racing game

(b) VR watching

(c) Video watching

(d) Phone calling

Figure 4. Selected trajectories of micromobility patterns

traces, occasional falls are observed but the signal strength quickly recovers after them. This is in close agreement with the beam center behavior reported in [23], where the center of the beam rarely fluctuated.

Visual analysis of the rest of the time series allows identification of the phone application as having lower received signal strength fluctuations as compared to VR watching and racing games. The maximum deviations observed for this application are generally limited to 15 dBm with an occasional drop of 30 dBm. The two remaining applications are characterized by visually similar behaviors with rapid variations. Nevertheless, as one may observe there are still large intervals for both VR watching and racing game applications, where the received signal strength remains relatively constant. This implies that the resources utilized for beam tracking may still be saved, even for these applications.

4. Communication system design

In this section, we focus on physical layer devices within coherent THz communication schemes with far-beyond-gigabit data rates. Classic microwave designs of direct conversion transmitters/receivers are briefly discussed together with their modern and actively developing radiophotonic alternatives. Path loss management via smart antenna devices embedded in reflection-aided ultra directional THz channels was further assessed in terms of radiophysics and engineering challenges.

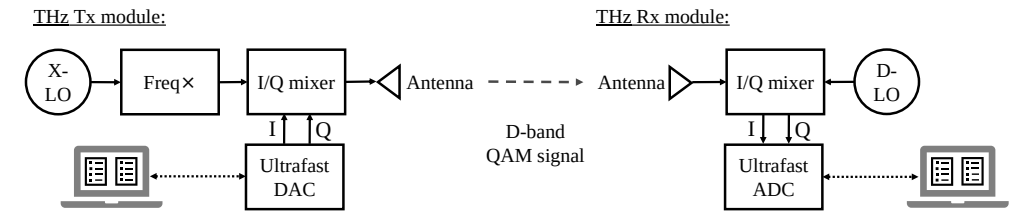

(a) Classic direct conversion with QAM modulation

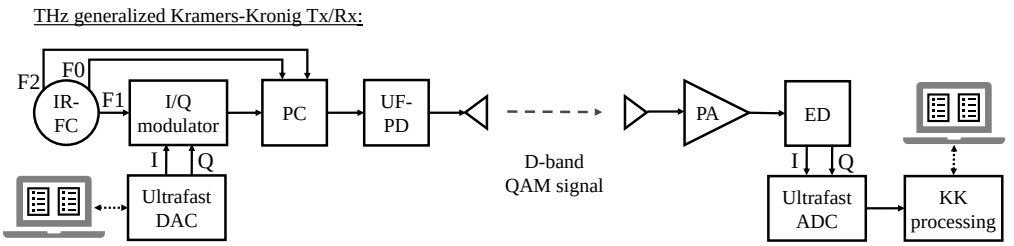

(b) Radiophotonic conversion with QAM modulation

Figure 5. Coherent THz communication schemes

4.1. Physical layer and direct conversion schemes

It is conventionally stated that the higher the carrier frequency in the communication channel, the larger the channel capacity. Considering the evolution of wireless networks, this statement can be recognized as a gradual migration of their operating frequencies from the L to D band over the last several decades. As expected, the technological background of the predecessor is not always easily adopted by the successor. This situation has several reasons that eventually originate from the available hardware fabrication and operation technologies. Currently, state-of-the-art wireless systems are being used in the THz technology. They are expected to occupy the D band, which is the lower part of the THz spectrum and spans from 110 to 170 GHz. For coherent communications, it should potentially enable baud rates of up to 55–85 GHz at the air interface. However, such a performance is only possible when wireless transceivers are compatible with the amplitude and phase manipulation methods at either i) the carrier frequency itself in the case of classic microwave modulation schemes or ii) higher-than-carrier frequencies if radiophotonic schemes are implemented [27, 28].

Quadrature amplitude modulation (QAM) schemes with 16–256 levels are commonly used in 4G/LTE and 5G systems. QAM schemes with up to 1024 modulation levels are expected to appear in 6G THz channels in the near future. Fig. 5 shows simplified examples of conventional and radiophotonic hardware implementations of coherent QAM-based THz communications. The fundamental difference between them is related to the manner in which a D-band QAM signal is generated and processed.

As shown in Fig. 5(a), the conventional method is to build a direct conversion transmitter/receiver channel with narrow-beam antenna front-ends. It utilizes four key analog elements, including X- and D-band local oscillators (X-LO and D-LO), an X-to-D-band frequency multiplication and amplification chain (Freq×), and two D-band in-phase/quadrature (I/Q) mixers, as well as two key digital elements, including ultrafast digital-to-analog and analog-to-digital converters (DAC and ADC). The robust

technology of X-LO acting as a fundamental frequency source is yttrium iron garnet (YIG) voltage-controlled oscillators (VCOs). When frequency- or phase-locked, 8–12 GHz YIG VCOs ensure high spectral purity with a phase noise close to the thermal limit of approximately −180 dBc/Hz above a corner frequency offset from the carrier and the output power beyond 13 dBm [29]. To elevate the generated X-band frequency to 140–150 GHz and an output power of 20–26 dBm, it is efficient to use Freq× with an A3B5-based frequency multiplier and power amplifier (PA) circuits [30] which can be tuned and cascaded to meet the desired specifications. Coding and decoding of D-band carrier signal within communication schemes with I/Q modulation ensure data rates beyond 50 Gbit/s in short distance links for Monolithic Microwave Integrated Circuits (MMICs) based on Fin Field Effect Transistor (FinFET) Complementary Metal Oxide Semiconductor (CMOS), SiGe Bipolar CMOS (BiCMOS), and SiGe Heterojunction Bipolar Transistor (HBT) platforms [31–33]. Further increases in the communication range and data transfer rates are possible if the signal strength and baud rates are increased beyond 1 W and 30 GHz levels. This, in turn, can be accomplished by replacing intrinsically limited Si-based electronics with more capable A3B5 devices [34].

The radiophonic generation and processing of THz carrier signals are also considered promising. Referring to Fig. 5(b), the I/Q modulation of the infrared frequency comb (IR-FC) components can be used, followed by their summation and downconversion with the aid of a fiber-optic power combiner (PC) and ultrafast photodiode (UF-PD). This approach enables the simple implementation of QAM modulation, which is capable of providing a high data rate and high spectral efficiency. The coherent reception of data signals at THz frequencies is possible within a simplified implementation scheme that relies on the use of an envelope detector (ED) and subsequent digital signal processing. This scheme enables the restoration of the phase of the original signal from the envelope measurements and is a variation of the Kramers-Kronig (KK) receiver. Its application made it possible to achieve the highest data transfer rate, namely, 115 Gbit/s for a 110 m channel [35], demonstrated for wireless D-band communications. The choice of ED technology in the KK receiver scheme affects the resource intensity of the transmitter/receiver fabrication and operation. In addition, it affects the complexity of generalizing the algorithm for digital processing at Rx back-end which ensures high-speed data transfer, with a low error rate.

We propose combining the features of electronic and photonic integrated circuits (ePICs) to facilitate the creation of an ultrawideband I/Q mixer that is compatible with the GaAs-on-Si platform. Our GaAs-on-Si I/Q mixer utilizes a multistage Y-junction-based power distribution network (PDN) to couple LO and carrier signals with I/Q mixing elements. The PDN was implemented in a 500 μm thick high-resistivity Si by creating a perforated dielectric structure exhibiting permittivity anisotropy and pronounced single-mode propagation paths [36]. Propagating THz was delivered to two diode-loaded tapered slot lines (TSLs) implemented on top of the single-mode waveguides of the PDN. To improve the coupling, the waveguides were terminated using a pair of distributed Brag reflectors. The I/Q control and readout signals are delivered through 2 50-Ohm slot lines connected to the rear ends of the TSLs. The diodes rely on the n+/n/etch-stopper/handle GaAs heterostructure, enabling face-down attachment to the Si wafer with further removal of the handle and etch-stopper layers before structuring the n/n+ bilayer [37]. To reduce the parasitic capacitances in the diode intrinsic circuitry, a gamma-shaped anode-suspended bridge can be implemented [38].

The expected performance and technological feasibility of the proposed ePIC for a D-band I/Q mixer were assessed in [39]. The performance simulations use numerical S-parameter analyses similar to those described in detail elsewhere [40].

The developed PDN of the mixer ePIC utilizes a constant waveguide cross-section of $0.29\lambda_0 \times 0.23\lambda_0$ along all the single-mode propagation paths. In turn, the circular segments of the integrated Y-junctions have radii of curvature of $0.69\lambda_0$ with λ_0 presenting a free-space wavelength of electromagnetic radiation. To implement a 90-degree lag in the phase required for quadrature up-

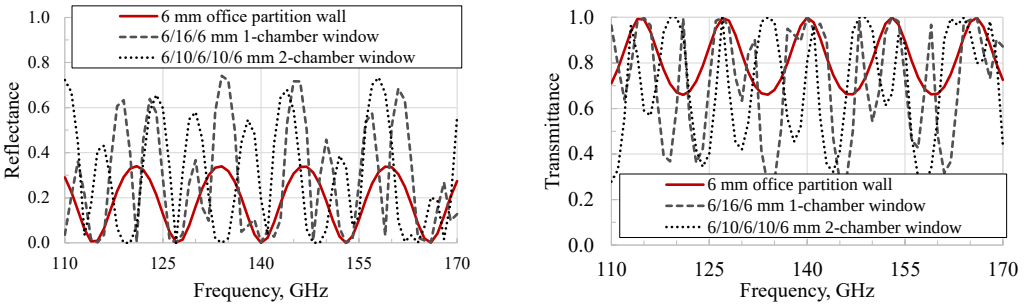

(a) Reflection spectra **(b)** Transmission spectra

Figure 6. Properties of inner and outer glass elements of the office

and down-conversions, two straight waveguide sections of different optical lengths are incorporated into the Y-junction adjacent to the LO input. Such a geometry in the first-run design ensures 7–8 dB of insertion losses for the LO and carrier signals including 1.5 dB intrinsically attributed to the transitions from PDN single-mode waveguides to diode-loaded TSLs. The corresponding reflection losses reach 28 dB whereas the isolation exceeds 13–16 dB. For carrier frequencies between 135–145 GHz, a phase difference of 89 ± 5 deg and an amplitude imbalance close to 1 dB were maintained between the I and Q mixing elements. In terms of packaging, the mixer is compatible with the WR6.5 waveguide at the UG387 flange as an input-output LO/carrier signal interface. A coaxial SMA/SMP interface was chosen for the control and readout of the I and Q states. On-chip integration with V/Q-band GaAs Schottky diode frequency multipliers [41] was also possible. Moreover, given the technological robustness of integrated Si photonic crystals of up to a few terahertz [40, 42], the feasibility of the design for D-band operation is evident. Prototyping and a detailed inspection of the forecasted mixer performance at 110-170 GHz are among our future plans.

4.2. Reflection-aided channels

Given the severe attenuation by high-humidity outdoor environments and the limitation of available carrier power, D-band 6G systems have been widely proposed for indoor ultra directional data links. However, such deployments are characterized by occasional distortions of the wireless signal upon interaction with moving users or static furniture-filling premises. Knowing the radiophysical properties of construction materials, one can find a sweet spot for placing a pencil-beam transmitter to meet the desired needs of single- and multi-user scenarios. For instance, as shown in Fig. 6, the same inner and outer flat glass elements typical of modern workspaces can effectively behave under the deployment of either LoS or reflection-aided links if the carrier frequency is shifted by 2–5% only.

Using the THz reflectometry together with characteristic matrix (CM) analysis of layered dielectric media [43], we extracted the complex permittivities of widely used construction materials, including flat glass, drywall, and aerated concrete [44]. We experimentally assessed the accuracy of the Fresnel equations (FE) and found that pronounced self-interference may potentially lead to an increase in calculation error up to 14.4–29.1%. The accuracy of FE was quantified using the normalized mean squared deviation (NMSD) of the calculated reflectances from their frequency profiles forecasted by permittivity-based CM analysis. A comparison was performed for s- and p-polarized signals in the frequency range of 130–160 GHz with the angle of incidence approaching Brewster's angle. As

Table 2

Material-dependent accuracy of reflectance calculations via FE

Type of material	Permittivity	NMSD(s)	NMSD(p)
Glass	$7.23+0.22i$	0.012	0.065
Drywall	$2.63+0.026i$	0.144	0.291
Concrete	$1.9+0.017i$	0.002	0.003

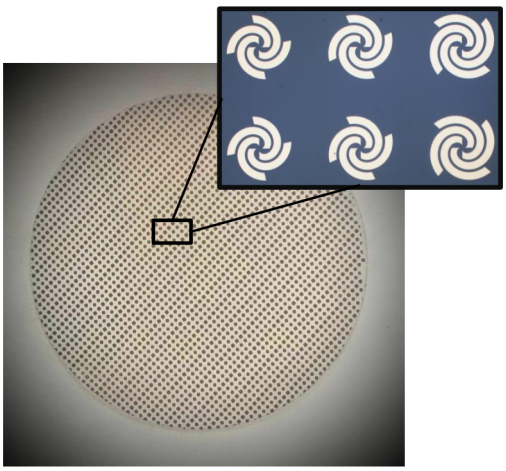

Figure 7. A 1k+ pixel static RIS for D-band operation

can be observed from Tab. 2, the accuracy is insufficient for precise channel modeling at the system level, and hybrid propagation models [45] must account for interference effects when scattering off furniture is considered.

As discussed earlier, the D-band wireless data links of 6G networks are vulnerable to dynamic signal blockage and user micromobility. This feature has an intrinsic nature and is attributed to the extreme directionality of the antenna elements at both the BS and UE operated at carrier frequencies of approximately 150 GHz. Efficient pencil-beam propagation management must be relied upon to eliminate signal fading and potential connection failure. Thus, a smart antenna environment is proposed as a promising solution to meet the demands of ultrawideband and stable communications in the D-band or beyond.

RIS-aided D-band communication technologies are expected to be deployed in three logical steps, starting with the adoption of static RISs by the 5/6G architectures with their further replacement by semi-static and dynamically controlled RIS modules. Although continuous beam steering with a wide angular field of view is attractive, practical systems are also seriously judged by their cost and operation efficiencies. Thus, technologically robust multi-state fast-beam steerers are of particular interest to commercial system developers.

Fig. 7 shows an image of a static RIS designed for operation at 150 GHz. It relies on a 140 μm thick quartz wafer with a two-sided metallization system. The rear side metallization was implemented in the form of a wafer-sized circular screen that acted as a ground plane. The front side is covered by a spiral-based periodic array structure with uniform amplitude and spacing, which utilizes more

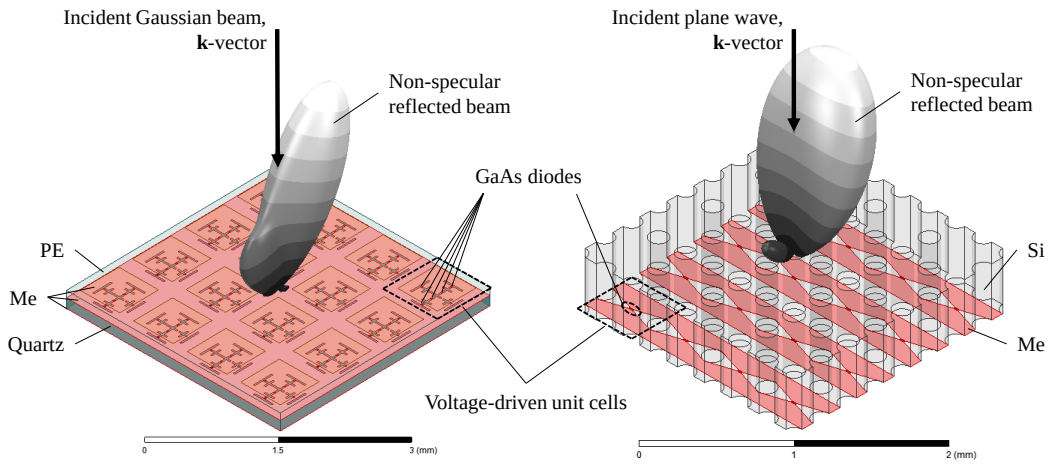

(a) 2-bit RIS: electronic 16px cell **(b)** 1-bit RIS: photonic-electronic 16px cell

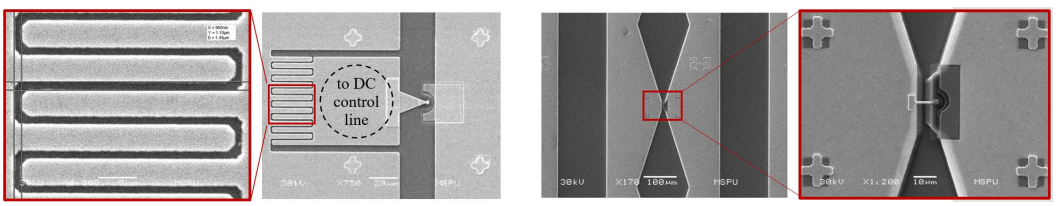

(c) 2-bit RIS: embedded tuning diodes **(d)** 1-bit RIS: embedded tuning diodes

Figure 8. Multi-state dynamic RISs for D-band operation

than 1000 (1k+) identical elements. The array phase increment of 120 deg results in a deflection angle of 50 deg as compared to the case of specular reflections. This design ensures operation at angles of incidence within ±75 deg supporting both linear and circular polarizations. The reflection losses were below 1 dB and the cross-polarization level was −24 dB. This performance is in good agreement with the simulation results. The simulation sequence relies on numerical Floquet port analysis and analytical beam profile construction via the array factor method. The fabricated RIS sample was successfully used for the non-distortive repetition of a 6 deg wide Gaussian beam, as reported in detail elsewhere [46]. The developed passive platform is well-suited for further integration with lumped tuning elements. These elements, in turn, need to ensure system reconfiguration speed on a microsecond scale when dynamically controlled RISs are considered. This can be achieved by using high-speed transistors or diode electronics, which greatly outperform low-speed devices based on microelectromechanical systems, liquid crystals, and phase change materials [47]. However, the latter demonstrates acceptable speed and repeatability upon state cycling [48]. This makes them attractive candidates for power-efficient semi-static RIS modules.

In the THz research community, GaAs planar Schottky diodes (PSDs) are well recognized for their excellent performance as frequency multipliers and mixers in practical high-resolution spectral instruments [41]. Fig. 8 provides examples of their use as tuning elements in multi-state dynamic RISs designed for D-band operation. The design shown in Fig. 8(a) was inspired by the award-winning 2-bit RIS, supporting the linear and circular polarizations reported in [49]. The 2 major

modifications are introduced by us to make it technologically robust and well-suited for MMIC implementation [50]. First, the air gap under the patch-carrying upper substrate was eliminated. We also replaced the substrate with a lower-permittivity material, namely, 100 μm thick polyethylene (PE) film, to maintain proper electrical spacing to the metallic (Me) slotted screen with built-in diode elements. These elements were originally presented by positive-intrinsic-negative (PIN) diodes exhibiting performance degradation in the D-band. Thus, we replaced them with PSDs, whose junction transport properties were incorporated into the parameterized unit cell hybrid model through a voltage-dependent admittance, $\hat{Y}(V_b)$:

$$\hat{Y}(V_b) = \frac{d}{dV_b}\left(I_s \exp\left(\frac{V_b}{\eta V_t}\right) - I_s\right) + i\omega\frac{\pi d_j^2}{4}\sqrt{\frac{q\varepsilon N_d}{2(\psi_{bi} - V_b)}}.$$

Physical quantities attributed to the typical diode layered structure and operating regimes are tabulated along with the description of an auxiliary ABCD-matrix math in [51]. Regarding the RIS structure, the Me screen was implemented on top of a back-metalized 140 μm thick quartz wafer. Our first-run prototyping with beam pattern measurement at 150 GHz confirmed a simulated reflection loss of 2 dB. Moreover, we measured a far-field beamwidth of 2.5 deg for the developed 16-pixel (16px) passive platform illuminated by a 6 deg wide Gaussian beam. Although the design is intrinsically compatible with the GaAs-on-quartz platform [37] of PSDs, we found that the fabrication tolerances were quite tight in terms of the radiophysical properties of the integrated RIS structure. Thus, we have revised this by Fig. 8(b).

The revised RIS has 1-bit elements represented by GaAs quarter-wave photonic crystal cells integrated with PSD-loaded tapered slot lines. The elegance of this solution is related to the use of a GaAs wafer-thick RIS structure without mechanical lapping or substrate transfer onto a low-permittivity wafer upon fabrication. Using the developed structure as part of a reconfigurable metasurface, one can implement reflective and refractive angular scanning within 60° with signal attenuation on a decibel scale.

Our simulations were strengthened by the MMIC fabrication and RIS operation developments. Scanning electron microscopy (SEM) images of the fabricated nonlinear tuning elements for the 1- and 2-bit RIS designs discussed above are shown in Fig. 8(c)–(d). They rely on Schottky contacts with at the diameter $d_j = 3\,\mu$m implemented at the interface of Ti/Pt/Au and n-GaAs, which are doped by Si to the dopant level $N_d = 4 \times 10^{-17}$ cm^3. The developed fabrication process provided an ideality factor $\eta \approx 1.5$, saturation current $I_s \approx 10$ pA, and series resistance $R_s \approx 15$ Ohm. Only two direct current (DC) control lines per row are required to implement planar angular scanning in both the proposed designs. Moreover, in the case of a 1-bit RIS circuit, it is sufficient to use a dual-channel digital-to-analog converter (DAC), controlling odd and even pairs of rows connected in parallel. For non-specular reflective beam steering, a DC bias voltage of 1 V must be delivered to them out-of-phase. In-phase biasing or no bias ensures specular reflection. The fabricated 64-element MMIC of a 140–150 GHz 1-bit RIS demonstrates decent stability when operated directly by a field-programmable gate array (FPGA) board equipped with a digital user interface and 2 50 MHz DAC channels. The normalized Allan variances were equal to 1×10^{-8} and 4×10^{-9} at integration times of 20 ms and 1 s, respectively. The consumed DC power is 13.7 mW, which corresponds to 219 mW when the number of RIS elements is increased to 1024. Such performance is on par with the power efficiency of D-band integrated transceivers relying on the SiGe BiCMOS platform [32]. It is also worth noting that the design bears structural similarity to the varactor-embedded reconfigurable metasurface recently proposed for X-band reflection-aided channels [52]. Thus, continuous beam steering can be implemented after minor tunings.

5. Conclusions

The THz frequency band is commonly considered an enabler for 6G communication systems. However, in addition to promises to deliver even more bandwidth to the air interface compared to mmWave 5G, it also brings novel challenges related to system design.

This paper aims to report on the current state-of-the-art channel characterization and communication system design. With respect to the former, we summarized recent results related to characterizing the dynamic human blockage and micromobility dynamics in LoS and nLoS THz channels. Then, we highlighted the challenges and discussed progress in electronics development, including the development of RIS intended for blockage avoidance in reflection-aided THz links.

Author Contributions: Conceptualization, G.G. and A.S.; methodology, A.P.; software, E.M.; validation, V.B., A.K. and M.E.; formal analysis, V.B.; investigation, A.K.; resources, A.P.; data curation, E.P.; writing—original draft preparation, A.S.; writing—review and editing, A.S.; visualization, E.M.; supervision, E.K.; project administration, G.G.; funding acquisition, E.K. All authors have read and agreed to the published version of the manuscript.

Data Availability Statement: Data sharing is not applicable.

Conflicts of Interest: The authors declare no conflict of interest.

Funding: This paper has been supported by the Russian Science Foundation, projects no. 22-79-10128 (Sections 1–2) and no. 22-79-10279 (Section 4). The studies reported in Section 3 has been conducted as a part of strategic project "Digital Transformation: Technologies, Effectiveness, Efficiency" of Higher School of Economics development programme granted by Ministry of science and higher education of Russia "Priority-2030" grant as a part of "Science and Universities" national project. Support from the Basic Research Program of the National Research University Higher School of Economics is also gratefully acknowledged.

References

1. Park, J.-J., Lee, J., Liang, J., Kim, K.-W., Lee, K.-C. & Kim, M.-D. *Millimeter wave vehicular blockage characteristics based on 28 GHz measurements* in *2017 IEEE 86th Vehicular Technology Conference (VTC-Fall)* (2017), 1–5.
2. Begishev, V., Sopin, E., Moltchanov, D., Kovalchukov, R., Samuylov, A., Andreev, S., Koucheryavy, Y. & Samouylov, K. Joint use of guard capacity and multiconnectivity for improved session continuity in millimeter-wave 5G NR systems. *IEEE Transactions on Vehicular Technology* **70,** 2657–2672 (2021).
3. Kovalchukov, R., Moltchanov, D., Begishev, V., Samuylov, A., Andreev, S., Koucheryavy, Y. & Samouylov, K. *Improved session continuity in 5G NR with joint use of multi-connectivity and guard bandwidth* in *2018 IEEE Global Communications Conference (GLOBECOM)* (2018), 1–7.
4. Begishev, V., Sopin, E., Moltchanov, D., Pirmagomedov, R., Samuylov, A., Andreev, S., Koucheryavy, Y. & Samouylov, K. Performance analysis of multi-band microwave and millimeter-wave operation in 5G NR systems. *IEEE Transactions on Wireless Communications* **20,** 3475–3490 (2021).
5. Sopin, E., Moltchanov, D., Daraseliya, A., Koucheryavy, Y. & Gaidamaka, Y. User association and multi-connectivity strategies in joint terahertz and millimeter wave 6G systems. *IEEE Transactions on Vehicular Technology* **71,** 12765–12781 (2022).
6. Zhang, H., Shlezinger, N., Guidi, F., Dardari, D., Imani, M. F. & Eldar, Y. C. Beam focusing for near-field multiuser MIMO communications. *IEEE Transactions on Wireless Communications* **21,** 7476–7490 (2022).
7. Durnin, J., Miceli, J. & Eberly, J. H. Comparison of Bessel and Gaussian beams. *Optics letters* **13,** 79–80 (1988).

8. Shurakov, A., Moltchanov, D., Prikhodko, A., Khakimov, A., Mokrov, E., Begishev, V., Belikov, I., Koucheryavy, Y. & Gol'tsman, G. Empirical blockage characterization and detection in indoor sub-THz communications. *Computer Communications* **201,** 48–58. doi:10.1016/j.comcom.2023.01.017 (2023).
9. Xing, Y. & Rappaport, T. S. *Propagation measurement system and approach at 140 GHz-moving to 6G and above 100 GHz* in *2018 IEEE global communications Conference (GLOBECOM)* (2018), 1–6.
10. Eckhardt, J. M., Petrov, V., Moltchanov, D., Koucheryavy, Y. & Kürner, T. Channel Measurements and Modeling for Low-Terahertz Band Vehicular Communications. *IEEE Journal on Selected Areas in Communications* **39,** 1590–1603 (2021).
11. Petrov, V., Eckhardt, J. M., Moltchanov, D., Koucheryavy, Y. & Kurner, T. *Measurements of reflection and penetration losses in low terahertz band vehicular communications* in *2020 14th European Conference on Antennas and Propagation (EuCAP)* (2020), 1–5.
12. Du, K., Ozdemir, O., Erden, F. & Guvenc, I. Sub-Terahertz and mmWave Penetration Loss Measurements for Indoor Environments. *arXiv preprint arXiv:2103.02745* (2021).
13. Kokkoniemi, J., Lehtomäki, J., Petrov, V., Moltchanov, D. & Juntti, M. *Frequency domain penetration loss in the terahertz band* in *2016 Global Symposium on Millimeter Waves (GSMM) & ESA Workshop on Millimetre-Wave Technology and Applications* (2016), 1–4.
14. Xing, Y. & Rappaport, T. S. *Propagation measurement system and approach at 140 GHz-moving to 6G and above 100 GHz* in *2018 IEEE global communications Conference (GLOBECOM)* (2018), 1–6.
15. Bilgin, B. A., Ramezani, H. & Akan, O. B. *Human blockage model for indoor terahertz band communication* in *2019 IEEE International Conference on Communications Workshops (ICC Workshops)* (2019), 1–6.
16. Shurakov, A., Rozhkova, P., Khakimov, A., Mokrov, E., Prikhodko, A., Begishev, V., Koucheryavy, Y., Komarov, M. & Gol'tsman, G. Dynamic Blockage in Indoor Reflection-Aided Sub-Terahertz Wireless Communications. *IEEE Access* **11,** 134677–134689. doi:10.1109/ACCESS.2023.3337050 (2023).
17. Ostrikova, D., Beschastnyi, V., Moltchanov, D., Gaidamaka, Y., Koucheryavy, Y. & Samouylov, K. System-level analysis of energy and performance trade-offs in mmWave 5G NR systems. *IEEE Transactions on Wireless Communications* (2023).
18. Balanis, C. Antenna theory: analysis and design. *Microstrip Antennas, John Wiley & Sons* (2005).
19. Ichkov, A., Gehring, I., Mähönen, P. & Simić, L. *Millimeter-wave beam misalignment effects of small-and large-scale user mobility based on urban measurements* in *Proceedings of the 5th ACM Workshop on Millimeter-Wave and Terahertz Networks and Sensing Systems* (2021), 13–18.
20. Petrov, V., Moltchanov, D., Koucheryavy, Y. & Jornet, J. M. *The effect of small-scale mobility on terahertz band communications* in *Proceedings of the 5th ACM International Conference on Nanoscale Computing and Communication* (2018), 1–2.
21. Petrov, V., Moltchanov, D., Koucheryavy, Y. & Jornet, J. M. Capacity and outage of terahertz communications with user micro-mobility and beam misalignment. *IEEE Transactions on Vehicular Technology* **69,** 6822–6827 (2020).
22. Stepanov, N., Turlikov, A., Begishev, V., Koucheryavy, Y. & Moltchanov, D. *Accuracy assessment of user micromobility models for thz cellular systems* in *Proceedings of the 5th ACM Workshop on Millimeter-Wave and Terahertz Networks and Sensing Systems* (2021), 37–42.
23. Stepanov, N., Moltchanov, D., Begishev, V., Turlikov, A. & Koucheryavy, Y. Statistical analysis and modeling of user micromobility for THz cellular communications. *IEEE Transactions on Vehicular Technology* **71,** 725–738 (2021).
24. Moltchanov, D., Gaidamaka, Y., Ostrikova, D., Beschastnyi, V., Koucheryavy, Y. & Samouylov, K. Ergodic outage and capacity of terahertz systems under micromobility and blockage impairments. *IEEE Transactions on Wireless Communications* **21,** 3024–3039 (2021).

25. Dugaeva, S., Begishev, V., Mokrov, E. & Samouylov, K. *Using Motion Sensors For Improved Beam Tracking in THz Communications with User Micromobility* in *2022 International Conference on Modern Network Technologies (MoNeTec)* (2022), 1–8.
26. Dugaeva, S., Begishev, V. & Stepanov, N. *Utilization of Machine Learning Algorithms to Identify User Applications* in *International Conference on Distributed Computer and Communication Networks* (2023), 410–422.
27. Du Preez, J., Sinha, S. & Sengupta, K. SiGe and CMOS technology for state-of-the-art millimeter-wave transceivers. *IEEE Access* (2023).
28. Jia, S., Lo, M.-C., Zhang, L., Ozolins, O., Udalcovs, A., Kong, D., Pang, X., Guzman, R., Yu, X., Xiao, S., *et al.* Integrated dual-laser photonic chip for high-purity carrier generation enabling ultrafast terahertz wireless communications. *Nature communications* **13,** 1388 (2022).
29. Gupta, A. S., Howe, D. A., Nelson, C., Hati, A., Walls, F. L. & Nava, J. F. High spectral purity microwave oscillator: Design using conventional air-dielectric cavity. *IEEE Transactions on Ultrasonics, Ferroelectrics, and Frequency control* **51,** 1225–1231 (2004).
30. Makhlouf, S., Cojocari, O., Hofmann, M., Nagatsuma, T., Preu, S., Weimann, N., Hübers, H.-W. & Stöhr, A. Terahertz sources and receivers: From the past to the future. *IEEE Journal of Microwaves* **3,** 894–912 (2023).
31. Brown, T. W., Dogiamis, G. C., Yeh, Y.-S., Correas-Serrano, D., Rane, T. S., Ravikumar, S., Chou, J. C., Neeli, V. B., Koo, J., Marulanda, M., *et al.* A 50-Gb/s 134-GHz 16-QAM 3-m dielectric waveguide transceiver system implemented in 22-nm FinFET CMOS. *IEEE Solid-State Circuits Letters* **4,** 206–209 (2021).
32. Carpenter, S., Zirath, H., He, Z. S. & Bao, M. A fully integrated D-band direct-conversion I/Q transmitter and receiver chipset in SiGe BiCMOS technology. *Journal of Communications and Networks* **23,** 73–82 (2021).
33. Rodríguez-Vázquez, P., Grzyb, J., Heinemann, B. & Pfeiffer, U. R. A 16-QAM 100-Gb/s 1-M wireless link with an EVM of 17% at 230 GHz in an SiGe technology. *IEEE Microwave and Wireless Components Letters* **29,** 297–299 (2019).
34. Gustavsson, U., Frenger, P., Fager, C., Eriksson, T., Zirath, H., Dielacher, F., Studer, C., Pärssinen, A., Correia, R., Matos, J. N., *et al.* Implementation challenges and opportunities in beyond-5G and 6G communication. *IEEE Journal of Microwaves* **1,** 86–100 (2021).
35. Harter, T., Füllner, C., Kemal, J. N., Ummethala, S., Steinmann, J. L., Brosi, M., Hesler, J. L., Bründermann, E., Müller, A.-S., Freude, W., *et al.* Generalized Kramers–Kronig receiver for coherent terahertz communications. *Nature Photonics* **14,** 601–606 (2020).
36. Shurakov, A., Prikhodko, A., Belikov, I. & Gol'tsman, G. *Terahertz Hot Electron Bolometer Coherent and Direct Detectors Utilizing Si Waveguiding Structures* in *2022 IEEE 8th All-Russian Microwave Conference (RMC)* (2022), 19–22.
37. Alijabbari, N., Bauwens, M. F. & Weikle, R. M. Design and characterization of integrated submillimeter-wave quasi-vertical Schottky diodes. *IEEE Transactions on Terahertz Science and Technology* **5,** 73–80 (2014).
38. Shurakov, A., Mikhailov, D., Belikov, I., Kaurova, N., Zilberley, T., Prikhodko, A., Voronov, B., Vasil'evskii, I. & Goltsman, G. *Planar Schottky diode with a Γ-shaped anode suspended bridge* in *Journal of Physics: Conference Series* **1695** (2020), 012154.
39. Shurakov, A., Belikov, I., Prikhodko, A. & Gol'tsman, G. *Photonic-Electronic IC of a Subterahertz GaAs-on-Si IQ mixer* in *2024 49th International Conference on Infrared, Millimeter, and Terahertz Waves (IRMMW-THz)* (2024 (to be published)).
40. Shurakov, A., Belikov, I., Prikhodko, A., Ershova, M. & Goltsman, G. Superconducting Electronic–Photonic Platform for HEB-Based Terahertz Spectrometers. *Applied Sciences* **13,** 5892 (2023).

41. Mehdi, I., Siles, J. V., Lee, C. & Schlecht, E. THz diode technology: Status, prospects, and applications. *Proceedings of the IEEE* **105,** 990–1007 (2017).
42. Koala, R. A., Fujita, M. & Nagatsuma, T. Nanophotonics-inspired all-silicon waveguide platforms for terahertz integrated systems. *Nanophotonics* **11,** 1741–1759 (2022).
43. Born, M. & Wolf, E. *Principles of optics: electromagnetic theory of propagation, interference and diffraction of light* (Elsevier, 2013).
44. Shurakov, A., Rozhkova, P., Khakimov, A., Mokrov, E., Prikhodko, A., Begishev, V., Koucheryavy, Y., Komarov, M. & Gol'tsman, G. Dynamic Blockage in Indoor Reflection-Aided Sub-Terahertz Wireless Communications. *IEEE Access* **11,** 134677–134689 (2023).
45. Gargari, A. A., Polese, M. & Zorzi, M. *Full-stack comparison of channel models for networks above 100 GHz in an indoor scenario* in *Proceedings of the 5th ACM Workshop on Millimeter-Wave and Terahertz Networks and Sensing Systems* (2021), 43–48.
46. Razakova, A., Prikhodko, A., Lvov, A., Shurakov, A. & Gol'tsman, G. Subterahertz circularly polarized 1k-pixel reflective surface for 6G applications. *St. Petersburg Polytechnic University Journal - Physics and Mathematics* (2024, to be published).
47. Fu, X., Yang, F., Liu, C., Wu, X. & Cui, T. J. Terahertz beam steering technologies: from phased arrays to field-programmable metasurfaces. *Advanced optical materials* **8,** 1900628 (2020).
48. Kozyukhin, S. A., Lazarenko, P. I., Popov, A. I. & Eremenko, I. L. Phase change memory materials and their applications. *Russ. Chem. Rev* **91,** 9 (2022).
49. Dai, L., Wang, B., Wang, M., Yang, X., Tan, J., Bi, S., Xu, S., Yang, F., Chen, Z., Di Renzo, M., *et al.* Reconfigurable intelligent surface-based wireless communications: Antenna design, prototyping, and experimental results. *IEEE access* **8,** 45913–45923 (2020).
50. Shurakov, A., Prikhodko, A., Belikov, I., Razakova, A. & Gol'tsman, G. *Integrated Circuit of an Intelligent Reflecting Surface for sub-THz Wireless Communication* in *2023 IEEE 18th International Conference on Nano/Micro Engineered and Molecular Systems (NEMS)* (2023), 183–187.
51. Prikhodko, A., Yaropolov, T., Shurakov, A. & Gol'tsman, G. *Unit cell model of a terahertz intelligent reflecting surface with Schottky microcontacts* in *35th European Modeling and Simulation Symposium (EMSS 2023)* (2023), 019.
52. Ratni, B., de Lustrac, A., Piau, G.-P. & Burokur, S. N. Active metasurface for reconfigurable reflectors. *Applied Physics A* **124,** 1–8 (2018).

Information about the authors

Shurakov, Alexander S.—PhD, Associate Professor, Department of General and Experimental Physics, Moscow Pedagogical State University (e-mail: alexander@rplab.ru, phone: +7 (499) 766-48-87, ORCID: 0000-0002-4671-7731, ResearcherID: E-4118-2014, Scopus Author ID: 55266061300)

Mokrov, Evgeny V.—Candidate of Physical and Mathematical Sciences, Senior lecturer of Department of Probability Theory and Cyber Security of Peoples' Friendship University of Russia (RUDN University) (e-mail: mokrov-ev@rudn.ru, phone: +7 (495) 952-28-23, ORCID: 0000-0003-3290-4541, ResearcherID: AAK-6348-2021, Scopus Author ID: 56512031300)

Prikhodko, Anatoliy N.—Junior Researcher, Specialized Department of Quantum Optics and Telecommunications of Scontel CJSC, HSE University (e-mail: anprihodko@hse.ru, phone: +7 (495) 772-95-90, ORCID: 0000-0002-4859-8975, ResearcherID: ADC-0507-2022, Scopus Author ID: 57207500541)

Ershova, Margarita I.—Junior Researcher, Laboratory of quantum detectors, Moscow Pedagogical State University (e-mail: mi.ershova@mpgu.su, phone: +7 (499) 766-48-87, ORCID: 0009-0009-6785-4389, ResearcherID: JNB-5214-2023, Scopus Author ID: 58298409900)

Begishev, Vyacheslav O.—Candidate of Physical and Mathematical Sciences, Assistant professor of the Department of Probability Theory and Cyber Security of Peoples' Friendship University of Russia (RUDN University) (e-mail: begishev-vo@rudn.ru, phone: +7 (495) 952-28-23, ORCID: 0000-0002-7232-4157, ResearcherID: AAF-6491-2019, Scopus Author ID: 56562837400)

Khakimov, Abdukodir A.—Candidate of Technical Sciences, Junior researcher of the Department of Probability Theory and Cyber Security of Peoples' Friendship University of Russia (RUDN University) (e-mail: khakimov-aa@rudn.ru, phone: +7 (495) 952-28-23, ORCID: 0000-0003-2362-3270, ResearcherID: AAD-1134-2019, Scopus Author ID: 57194233776)

Koucheryavy, Yevgeny A.—Doctor of Technical Sciences, Professor of the Department of Probability Theory and Cyber Security of Peoples' Friendship University of Russia (RUDN University) (e-mail: kucheryavyy-ea@rudn.ru, phone: +7 (495) 952-28-23, ORCID: 0000-0003-3976-2971, ResearcherID: D-7976-2018, Scopus Author ID: 6507253900)

Gol'tsman, Gregory N.—Doctor of Physical and Mathematical Sciences, Head of Department, Department of General and Experimental Physics, Moscow Pedagogical State University (e-mail: goltsman@rplab.ru, phone: +7 (499) 766-48-87, ORCID: 0000-0002-1960-9161, ResearcherID: A-4189-2014, Scopus Author ID: 7006771637)

UDC 004.2, 004.7
PACS 07.05.Tp
DOI: 10.22363/2658-4670-2024-32-2-181–201 EDN: CFLJNF

Текущеее состояние исследований в области моделирования каналов и разработки систем терагерцового диапазона

А. С. Шураков[1,2], Е. В. Мокров[3], А. Н. Приходько[1,2,4], М. И. Ершова[1], В. О. Бегишев[3], А. А. Хакимов[3], Е. А. Кучерявый[3], Г. Н. Гольцман[1,2,4]

[1] *Московский педагогический государственный университет, ул. Малая Пироговская, д. 1, стр. 1, Москва, 119991, Российская Федерация*
[2] *Национальный исследовательский университет «Высшая школа экономики», ул. Мясницкая улица, д. 20, Москва, 101000, Российская Федерация*
[3] *Российский университет дружбы народов, ул. Миклухо-Маклая, д. 6, Москва, 117198, Российская Федерация*
[4] *Российский квантовый центр, Сколково, 143025, Российская Федерация*

Аннотация. На текущий момент стандартизация систем 5G Новое Радио, работающих в диапазоне частот микро- и миллиметровых волн, завершена. Исследовательское сообщество, стандартизищирующие организации и производители оборудования начинают решать вопрос о том, какой может или должна быть система связи 6G. Хотя технологические особенности все еще находятся на ранней стадии разработки, существует общее мнение, что эти системы будут использовать нижнюю часть терагерцового диапазона, 100–300 ГГц. Этот диапазон создает ряд специфических проблем для разработчиков систем, включая эффекты, связанные с характеристиками канала, а также концептуально новые требования к электронике. Целью данной статьи является обзор текущего состояния исследований в области определения характеристик каналов и проектирования систем связи. В отношении первых мы будем рассматривать динамическую блокировку путей распространения сигнала телом человека и эффект микромобильность. С точки зрения системного уровня, мы концентрируемся на устройствах для схем прямого преобразования и разработке так называемых реконфигурируемых интеллектуальных поверхностей, которые потенциально могут служить экономичным методом устранения блокировок.

Ключевые слова: терагерцовый диапазон, 6G, блокировка, микромобильность, эксперимент, когерентная связь, прямое преобразование, реконфигурируемя интеллектуальная поверхность